







## Theoretical analysis of the extraction of neutron skin thickness from coherent $\pi^0$ photoproduction off nuclei

F. Colomer <sup>1,2</sup>, P. Capel <sup>1,2,\*</sup>, M. Ferretti,<sup>2</sup> J. Piekarewicz <sup>3,†</sup>, C. Sfienti <sup>2,‡</sup>, M. Thiel <sup>2,§</sup>, V. Tsaran,<sup>2</sup> and M. Vanderhaeghen <sup>2,¶</sup>

<sup>1</sup>*Physique Nucléaire et Physique Quantique, Université Libre de Bruxelles (ULB), B-1050 Brussels*

<sup>2</sup>*Institut für Kernphysik, Johannes Gutenberg-Universität Mainz, 55099 Mainz, Germany*

<sup>3</sup>*Department of Physics, Florida State University, Tallahassee, Florida 32306, USA*



(Received 3 May 2022; accepted 27 September 2022; published 18 October 2022)

**Background:** Coherent  $\pi^0$  photoproduction on heavy nuclei has been suggested as a reliable tool to infer neutron skin thicknesses. To this aim, various experiments have been performed, especially on  $^{208}\text{Pb}$ .

**Purpose:** We analyze the sensitivity of that reaction process to the nucleonic density, and especially to the neutron skin thickness, for  $^{12}\text{C}$ ,  $^{40}\text{Ca}$ , and  $^{208}\text{Pb}$ , for which reliable data exist, and on  $^{116,124}\text{Sn}$ , for which measurements have been performed in Mainz. We study also the role played by the  $\pi^0$ -nucleus final-state interaction.

**Methods:** A model of the reaction is developed at the impulse approximation considering either plane waves or distorted waves to describe the  $\pi^0$ -nucleus scattering in the outgoing channel.

**Results:** Our calculations are in good agreement with existing data, especially for  $^{208}\text{Pb}$ . The sensitivity of the theoretical cross sections to the choice of the nucleonic density is small and below the experimental resolution.

**Conclusions:** Coherent  $\pi^0$  photoproduction is mostly an isoscalar observable that bares no practical sensitivity to the neutron skin thickness. To infer that structure observable it should be coupled to other reaction measurements, such as electron scattering, or by comparing experiments performed on isotopes of the same chemical element.

DOI: [10.1103/PhysRevC.106.044318](https://doi.org/10.1103/PhysRevC.106.044318)

### I. INTRODUCTION

One of the major challenges of the 21st century in nuclear physics is the determination of the nuclear equation of state (EoS) and more specifically the density dependence of the symmetry energy [1,2]. The equation of state governs the structure of the densest objects in the universe, from the bulk properties of heavy nuclei up to the structure of neutron stars. This exciting field of research has led to the development of a large range of both observational and experimental techniques to constrain the EoS from both terrestrial measurements and multimessenger astronomy [1–3].

The asymmetry term of the EoS quantifies the energy cost of converting symmetric nuclear matter, where the number of neutrons equals that of protons, into pure neutron matter. The structure of neutron stars is strongly sensitive to the asymmetry term—and especially to its density dependence—because it provides the dominant contribution to the baryonic pressure in the vicinity of nuclear matter saturation density. Indeed, it has been argued that the pressure near twice saturation density sets the overall scale for stellar radii [4]. In heavy

nuclei with a significant neutron excess, the development of a *neutron skin* emerges from a competition between surface tension and the density dependence of the symmetry energy. In the context of the liquid-drop model, surface tension favors the creation of an incompressible drop with the smallest possible area. In contrast, the symmetry energy favors moving the excess neutrons from the core—where the asymmetry term is large—to the surface, where the asymmetry term is small. The difference between the value of the asymmetry term at the center of the nucleus relative to its value at the surface is denoted by  $L$ . As such, the *asymmetry pressure*  $L$  controls both the thickness of the neutron skin and the radius of a neutron star [5,6].

In the laboratory, the most direct way to constrain the asymmetry pressure is to measure the thickness of the neutron skin in heavy nuclei [1–3]. The neutron skin thickness is defined as the difference between the root-mean-square radius of the neutron density relative to that of the proton. That is,

$$R_{\text{skin}} = R_n - R_p = \sqrt{\langle r_n^2 \rangle} - \sqrt{\langle r_p^2 \rangle}. \quad (1)$$

For this study, the choice of  $^{208}\text{Pb}$  is optimal. It is stable, which makes it readily available for laboratory experiments, it exhibits a large neutron-proton asymmetry, and its heavy, doubly magic nature makes it amenable to mean-field calculations.

Various experimental techniques have been implemented to extract the neutron skin thickness of  $^{208}\text{Pb}$  [1–3]. Parity-violating elastic electron scattering is widely regarded as

\*pcapel@uni-mainz.de

†jpiekarewicz@fsu.edu

‡sfienti@uni-mainz.de

§thielm@uni-mainz.de

¶vandma00@uni-mainz.de

the cleanest experimental technique from which  $R_{\text{skin}}^{208}$  can be inferred. The original lead radius experiment (PREX) infers  $R_{\text{skin}}^{208} = 0.33_{-0.18}^{+0.16}$  fm [7], a value that has since been refined by the recent PREX-2 campaign to  $R_{\text{skin}}^{208} = 0.283 \pm 0.071$  fm [8]. Elastic proton-scattering experiments suggest a thinner neutron skin with a significantly smaller uncertainty, namely,  $R_{\text{skin}}^{208} = 0.211_{-0.063}^{+0.054}$  fm [9]. Antiprotonic atoms measurements have inferred an even smaller neutron skin of  $R_{\text{skin}}^{208} = 0.16 \pm 0.02(\text{stat.}) \pm 0.04(\text{syst.})$  fm [10,11]. To date, the smallest estimate of the neutron skin thickness of  $^{208}\text{Pb}$ ,  $R_{\text{skin}}^{208} = 0.156_{-0.021}^{+0.025}$  fm, was obtained from a measurement of the electric-dipole polarizability [12], a quantity that has been shown to be strongly correlated to the neutron skin thickness [13]. Although not fully inconsistent, these estimates spread over a broad range of values, leading to significant uncertainties in the inferred contribution of the asymmetry term to the nuclear EoS. The large spread is generated from the significant model dependence involved in the extraction of  $R_{\text{skin}}^{208}$  from the various experiments [3]. This is particularly true in the case of hadronic reactions that suffer from large systematic errors. To consistently compare this suite of laboratory experiments with recent astronomical observations it is imperative to properly quantify the systematic and model uncertainties. In this context, we note that the PREX error is dominated by *statistical* errors.

In this work we focus on another experimental method that has been suggested to pin down the value of the neutron skin thickness: the coherent  $\pi^0$  photoproduction. In such a reaction, an incident photon generates through its interaction with the target nucleus a neutral pion that can then be easily detected by its dominant  $2\gamma$  decay channel [14,15]. At the level of the plane-wave impulse approximation (PWIA), the cross section is directly proportional to the Fourier transform of the nuclear density [16]. An accurate measurement would give access to the entire baryon density and hence to an estimate of the neutron skin thickness, given that the proton density is well known from decades of electron-scattering experiments [17]. Measurements of coherent  $\pi^0$  photoproduction on different targets and at various photon energies already exist [18,19]. In one such analysis, Tarbert *et al.* have inferred a rather thin neutron skin thickness for  $^{208}\text{Pb}$  with a very small uncertainty:  $R_{\text{skin}}^{208} = 0.15 \pm 0.03(\text{stat.})_{-0.03}^{+0.01}(\text{syst.})$  fm [19]. Given the hadronic character of the production channel, the small systematic error seems unrealistic. Indeed, a theoretical analysis suggests that the uncertainty claimed by Tarbert *et al.* is significantly underestimated because of second-order effects that were not included in the model used to analyze the data [20].

Here we follow a complementary approach by studying in detail the sensitivity (or lack thereof) of the  $\pi^0$ -photoproduction cross section to the choice of nuclear density. Moreover, we also analyze the role played by the interaction between the pion and the nucleus in the final state. To reach this goal, we have written a reaction code based on the impulse approximation (IA) [16,21], which is used to analyze the experimental data [18,19]. In the impulse approximation, one assumes that the elementary  $\gamma N \rightarrow \pi^0 N$  interaction remains unchanged in the nuclear medium. The approach proposed here can examine the sensitivity of the cross

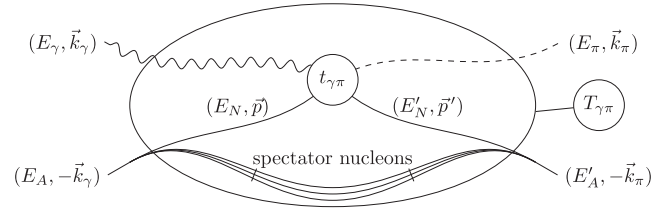


FIG. 1. Kinematics of the pion-photoproduction reaction on a nucleus in the  $\gamma$ - $A$  ( $\equiv \pi$ - $A$ ) rest frame described at the impulse approximation. The four-vectors of the photon, the nucleus before the reaction, the pion, and the nucleus after the reaction correspond to the indices  $\gamma$ ,  $A$ ,  $\pi$ , and  $A'$ , respectively. Inside the nucleus, the four-vectors of the struck nucleon before and after the reaction read  $(E_N, \vec{p})$  and  $(E'_N, \vec{p}')$ .

section to various choices of neutron densities as well as to the impact of  $\pi^0$ -nucleus final-state interactions by performing both plane-wave (PWIA) and distorted-wave (DWIA) calculations.

The model is briefly described in Sec. II and its predictions are confronted against existing experimental data on  $^{12}\text{C}$ ,  $^{40}\text{Ca}$ , and  $^{208}\text{Pb}$  [18] in Sec. III. In that section, the sensitivity of the theoretical cross sections to the choice of nuclear density is carefully analyzed and the role played by the  $\pi^0$ -nucleus interaction in the final state is investigated. The same model is then applied to two tin isotopes— $^{116}\text{Sn}$  and  $^{124}\text{Sn}$ —for which the  $\pi^0$ -photoproduction cross section has been measured at Mainz. Section IV summarizes our predictions for those two isotopes and estimates the experimental precision that must be reached to enable us to infer information about the evolution of the neutron skin thickness along the tin isotopic line. A brief summary and conclusions are presented in Sec. V.

## II. COHERENT $\pi^0$ PHOTOPRODUCTION AT THE IMPULSE APPROXIMATION

We consider the reaction induced by a photon  $\gamma$  on a nucleus  $A$  that produces a neutral pion  $\pi^0$  while leaving the nucleus in its initial ground state. This coherent  $\pi^0$ -photoproduction process reads

$$\gamma + A \rightarrow \pi^0 + A. \quad (2)$$

To model this reaction, we consider only the dominant one-body mechanism of photoproduction in which the neutral pion is produced on a single nucleon of the target  $A$ . Two-body processes, such as the one in which a charged pion is produced on a first nucleon and then charge exchanges into a neutral pion onto another nucleon, are neglected at the level of the impulse approximation adopted here [16,21].

A description of this reaction at the IA, including its relevant kinematics, is provided in Fig. 1: The initial photon of energy  $E_\gamma$  and momentum  $\vec{k}_\gamma$  within the  $\gamma$ - $A$  center-of-momentum frame collides with a nucleon  $N$  of energy  $E_N$  and momentum  $\vec{p}$ , producing the outgoing neutral pion  $\pi$  of energy  $E_\pi$  and momentum  $\vec{k}_\pi$ . The remaining  $A - 1$  nucleons in the target are treated as spectators. The process is coherent because the total amplitude is obtained as the sum over the

individual nucleon amplitudes. Furthermore, at the level of the impulse approximation, it is assumed that the elementary on-shell amplitude is unchanged in the nuclear medium; that is, as far as the elementary amplitude is concerned, the nucleons are treated as free. In the particular case of a spin-zero nucleus, the photoproduction amplitude for a photon of polarization  $\lambda$  reads [16]

$$U_{\gamma\pi}^{(\lambda)}(\vec{k}_\pi, \vec{k}_\gamma) = \frac{-i\lambda e^{i\phi\lambda}}{\sqrt{2}} \mathcal{W}_A [f_2^p(\vec{k}_\pi, \vec{k}_\gamma) \mathcal{F}[\rho_p](q) + f_2^n(\vec{k}_\pi, \vec{k}_\gamma) \mathcal{F}[\rho_n](q)], \quad (3)$$

where  $\vec{q} = \vec{k}_\pi - \vec{k}_\gamma$  is the momentum transferred during the process,  $\phi$  is the azimuthal angle of the outgoing pion relative to the incoming photon,  $\mathcal{W}_A$  is a phase-space factor that we choose identical to the one defined in Ref. [16],  $f_2^N$  are the elementary photoproduction amplitudes on a single nucleon, either proton ( $N = p$ ) or neutron ( $N = n$ ), and  $\mathcal{F}[\rho_N]$  are the Fourier transforms of the nucleonic densities:

$$\mathcal{F}[\rho_N](q) = \int e^{i\vec{q}\cdot\vec{r}} \rho_N(\vec{r}) d\vec{r}. \quad (4)$$

The elementary photoproduction amplitudes  $f_2^N$  are calculated in the  $\gamma$ - $A$  ( $\equiv \pi$ - $A$ ) rest frame as in Ref. [16]:

$$f_2^N(\vec{k}_\pi, \vec{k}_\gamma) = \frac{k_\pi k_\gamma}{\tilde{k}_\pi \tilde{k}_\gamma} \left( 1 + \frac{A-1}{2A} (\alpha_\gamma + \alpha_\pi) \right) \times \mathcal{F}_2^N(\tilde{\vec{k}}_\pi, \tilde{\vec{k}}_\gamma; W_{\gamma N}), \quad (5)$$

where the tilde on momenta denote momenta calculated in the  $\gamma$ - $N$  ( $\pi$ - $N$ ) rest frame as opposed to the  $\gamma$ - $A$  ( $\pi$ - $A$ ) frame, and  $\theta$  is the scattering angle in the  $\pi$ - $A$  rest frame. The coefficients  $\alpha_{\gamma(\pi)}$  are defined by the Lorentz transformations between the  $\gamma$ - $A$  ( $\pi$ - $A$ ) and  $\gamma$ - $N$  ( $\pi$ - $N$ ) frames as

$$\tilde{\vec{k}}_{\gamma(\pi)} = \vec{k}_{\gamma(\pi)} + \alpha_{\gamma(\pi)} \vec{P}, \quad (6)$$

where  $\vec{P} = \vec{k}_\gamma + \vec{p}$  ( $= \vec{k}_\pi + \vec{p}'$ ) is the total momentum of the  $\gamma$ - $N$  ( $\pi$ - $N$ ) system evaluated in the  $\gamma$ - $A$  ( $\pi$ - $A$ ) rest frame. Accordingly,  $\alpha_\gamma$  and  $\alpha_\pi$  are given by

$$\alpha_\gamma = \frac{1}{W_{\gamma N}} \left( \frac{\vec{P} \cdot \vec{k}_\gamma}{E_\gamma + E_N + W_{\gamma N}} - E_\gamma \right),$$

$$\alpha_\pi = \frac{1}{W_{\pi N}} \left( \frac{\vec{P} \cdot \vec{k}_\pi}{E_\pi + E'_N + W_{\pi N}} - E_\pi \right), \quad (7)$$

with  $W_{\gamma N}$  and  $W_{\pi N}$  being the  $\gamma$ - $N$  and  $\pi$ - $N$  relative energy, respectively. In this work, the standard CGLN amplitudes  $\mathcal{F}_2^N$  (Chew, Goldberger, Low, and Nambu [22]) are taken from the database MAID [23].

The coherent  $\pi^0$ -photoproduction cross section reads

$$\frac{d\sigma^{\gamma\pi}}{d\Omega} = \frac{k_\pi}{k_\gamma} \frac{1}{2} \sum_\lambda |T_{\gamma\pi}^{(\lambda)}|^2, \quad (8)$$

where  $T_{\gamma\pi}^{(\lambda)}$  is the  $T$  matrix for this process with an impinging photon of polarization  $\lambda$ . At the plane-wave impulse approximation (PWIA), the final-state interaction between the emitted

pion and the nucleus is neglected. The  $T$  matrix then simply equals the  $\pi^0$ -photoproduction amplitude  $U_{\gamma\pi}^{(\lambda)}$  (3)

$$T_{\gamma\pi}^{(\lambda)} \stackrel{\text{PWIA}}{=} U_{\gamma\pi}^{(\lambda)}. \quad (9)$$

Because the photoproduction amplitude  $U_{\gamma\pi}^{(\lambda)}$  depends linearly on the Fourier transforms  $\mathcal{F}[\rho_N]$  of the nucleonic densities, at the PWIA, the cross section for  $\pi^0$  photoproduction [Eq. (8)] should give us direct access to the nuclear density. In combination with charge density obtained, e.g., through electron elastic-scattering measurements [17], this observable could thus be used to infer information about the neutron distribution, and hence about the neutron skin thickness.

Final-state interactions have been shown to play a significant role in this reaction [16,18,21]. They can be taken into account at the distorted-wave impulse approximation (DWIA), within which the  $T$  matrix reads

$$T_{\gamma\pi}^{(\lambda)} \stackrel{\text{DWIA}}{=} U_{\gamma\pi}^{(\lambda)} - 4\pi \frac{A-1}{A} T_{\pi A} G_0 U_{\gamma\pi}^{(\lambda)}. \quad (10)$$

The first term corresponds to the PWIA term discussed above [see Eq. (3)], while the second accounts for the interaction of the  $\pi^0$  with the nucleus in the exit channel. The  $T$  matrix  $T_{\pi A}$  describes the  $\pi$ - $A$  scattering and is obtained by solving the Lippmann-Schwinger equation

$$T_{\pi A} = U_{\pi A} - 4\pi \frac{A-1}{A} U_{\pi A} G_0 T_{\pi A}, \quad (11)$$

where  $U_{\pi A}$  is an optical potential that simulates the  $\pi$ - $A$  interaction. We solve Eq. (11) through a partial-wave expansion following Ref. [24].

In both Eqs. (10) and (11),  $G_0$  is the free pion-nucleus propagator

$$G_0(k) = \frac{1}{2\mathcal{M}(k)} \frac{1}{E(k_0) - E(k) + i\epsilon}, \quad (12)$$

where  $\mathcal{M}$  is a relativistic equivalent of the  $\pi$ - $A$  reduced mass and is chosen as in Ref. [16].

The shape of the optical potential  $U_{\pi A}$  is chosen from Ref. [25] and will be later referred to as the MSU potential. In momentum space, its matrix elements for a pion scattered from  $\vec{k}_\pi$  to  $\vec{k}'_\pi$  read

$$U_{\pi A}(\vec{k}'_\pi, \vec{k}_\pi) = p_1 \bar{b}_0 \mathcal{F}[\rho](q_\pi) + p_2 B_0 \mathcal{F}[\rho^2](q_\pi) - \{p'_1 c_0 \mathcal{F}[\rho](q_\pi) + p'_2 C_0 \mathcal{F}[\rho^2](q_\pi)\} q_\pi^2 + (\vec{k}_\pi \cdot \vec{k}'_\pi) \mathcal{L}(q_\pi), \quad (13)$$

where  $\rho = \rho_p + \rho_n$  is the nucleonic density of  $A$ ,  $\vec{q}_\pi = \vec{k}'_\pi - \vec{k}_\pi$  is the transferred momentum, and the function  $\mathcal{L}$  is defined as

$$\mathcal{L}(q) = \mathcal{F} \left[ \frac{L}{1 + \frac{4\pi}{3} \lambda_{\text{LLEE}} L} \right] (q), \quad (14)$$

where  $\lambda_{\text{LLEE}}$  is the Lorenz-Lorentz-Ericson-Ericson parameter, first introduced in Ref. [26], and

$$L(r) = p_1^{-1} c_0 \rho(r) + p_2^{-1} C_0 \rho^2(r). \quad (15)$$

In all these expressions,  $p_1^{(\prime)}$  and  $p_2^{(\prime)}$  are kinematic factors whose expressions are

$$p_1 = \frac{1 + \varepsilon}{1 + \varepsilon/A}, \quad p_2 = \frac{1 + \varepsilon/2}{1 + \varepsilon/2A}, \quad (16)$$

$$p_1' = \frac{1}{2}(1 - p_1^{-1}), \quad p_2' = \frac{1}{2}(1 - p_2^{-1}), \quad (17)$$

where  $\varepsilon = (k_{\pi,0}^2 + m_\pi^2)^{1/2}/m_N$ , with  $k_{\pi,0}$  being the on-shell pion momentum. The values of the complex parameters  $\bar{b}_0$ ,  $c_0$ ,  $B_0$ ,  $C_0$ , and  $\lambda_{\text{LLEE}}$  are chosen identical to those of the set E in Ref. [25]. These values have been fit to reproduce elastic-scattering cross sections of charged pions measured at a laboratory kinetic energy of 50 MeV on several targets from  $^{12}\text{C}$  to  $^{208}\text{Pb}$ . This choice is therefore rather well suited for the purpose of this work.

### III. THEORETICAL ANALYSIS OF $\pi^0$ PHOTOPRODUCTION ON $^{12}\text{C}$ , $^{40}\text{Ca}$ , AND $^{208}\text{Pb}$

Krusche *et al.* have measured the cross section for coherent  $\pi^0$  photoproduction on several targets—including  $^{12}\text{C}$ ,  $^{40}\text{Ca}$ , and  $^{208}\text{Pb}$ —at an incoming photon energy of 200 MeV [18]. This constitutes an excellent set of data to which to compare the predictions of the model presented in Sec. II, explore the sensitivity of the calculations to the choice of the target densities, and analyze the impact of final-state interactions. For that last goal, we use the MSU potential [25], neglecting the small energy difference between its range of validity and the actual experimental conditions of Ref. [18]. Moreover, given that the neutron densities in both  $N = Z$  nuclei  $^{12}\text{C}$  and  $^{40}\text{Ca}$  are expected to follow closely the corresponding proton density, these two nuclei provide an excellent testing ground for assessing the role of final-state interactions.

#### A. Nucleonic densities

For our calculations on  $^{12}\text{C}$ , we consider three different choices of nuclear densities, which are displayed in Fig. 2 as a function of the radial distance  $r$ . The first one, shown in solid lines (with the proton density in black and the neutron density in red), is the phenomenological density of the São Paulo group [27]. It exhibits a simple Fermi-Dirac shape whose parameters have been adjusted by the known charge distributions inferred from electron-scattering experiments as well as theoretical densities derived from mean-field models across the entire nuclear chart. The second one is a density obtained by considering the nucleons to be bound in a mean-field harmonic oscillator (HO) potential well (dash-dotted line) [28]. The third density, plotted with dashed lines, corresponds to the charge distribution fit to reproduce electron-scattering data and parametrized with a Fourier-Bessel (FB) expansion [29]. For the HO and FB densities, we assume that  $\rho_n = \rho_p$ , which is sensible for this light, stable  $N = Z$  nucleus. Note that accurately calibrated mean-field models predict a very small and negative neutron skin thickness in  $^{12}\text{C}$  because of the Coulomb repulsion among protons. Both HO and FB densities exhibit nearly identical radial dependencies, in particular in the exponential tail. On the contrary, the São Paulo prediction differs significantly from the other two. Its  $p$  and

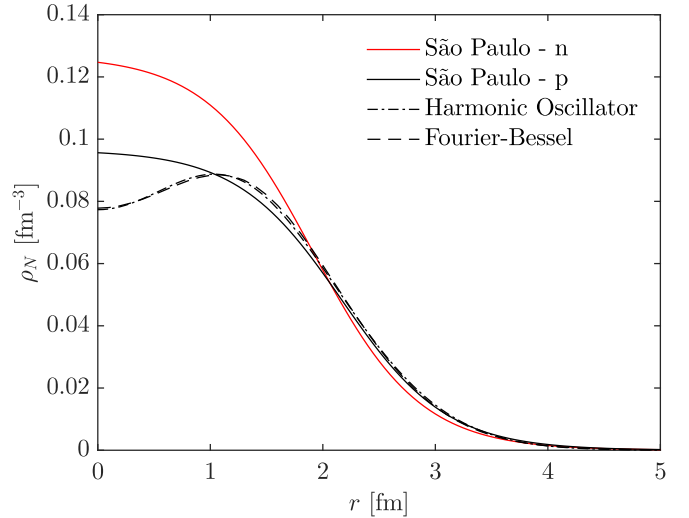


FIG. 2. Nucleonic densities of  $^{12}\text{C}$  considered in the calculations of the  $\pi^0$  photoproduction: the São Paulo parametrization (solid lines) [27], densities derived from a harmonic-oscillator mean field (dash-dotted line) [28], and those inferred from electron elastic scattering using a Fourier-Bessel expansion (dashed line) [29]. The São Paulo density differs for protons (black solid line) and neutrons (red solid line), whereas in the other cases, we assume  $\rho_n = \rho_p$ .

$n$  densities are very different from one another, a fact that is difficult to understand from the perspective of mean-field models. Whereas the proton density remains close to the HO and FB predictions beyond 1 fm, the  $n$  density decays too fast at large  $r$ , leading to an unrealistic *negative* neutron skin thickness. Nevertheless, we consider the São Paulo model to assess the sensitivity of the coherent process to the choice of densities. Moreover, this parametrization is available throughout the entire nuclear chart, which enables us to compare the calculations performed on different targets.

For the  $^{40}\text{Ca}$  target, in addition to the São Paulo and Fourier-Bessel parametrizations, we add predictions from relativistic mean-field calculations performed within the Florida State University (FSU) model of Ref. [30]. All three choices are displayed in Fig. 3. We follow the same line-type convention as in Fig. 2 for the first two. The FSU calculations have been performed with different choices of nonlinear coupling between the isoscalar and the isovector mesons to modify the neutron skin thickness of the nucleus without changing its isoscalar properties. Because these predictions are very close to one another, they are presented in Fig. 3 as bands: red for neutrons and gray for protons.

In this case, the differences between the three density choices is larger than for  $^{12}\text{C}$ . As such, it should help us assess the influence of this nuclear-structure observable—and in particular of the neutron skin thickness—on the  $\pi^0$ -photoproduction reaction. As for  $^{12}\text{C}$ , the São Paulo parametrization [27] predicts a very compact neutron density that decays much faster at large distances than  $\rho_p$  and than the other choices of densities. All FSU parametrizations predict very similar proton and neutron densities, with a slightly more compact  $\rho_n$  [30], leading to a slightly negative neutron skin

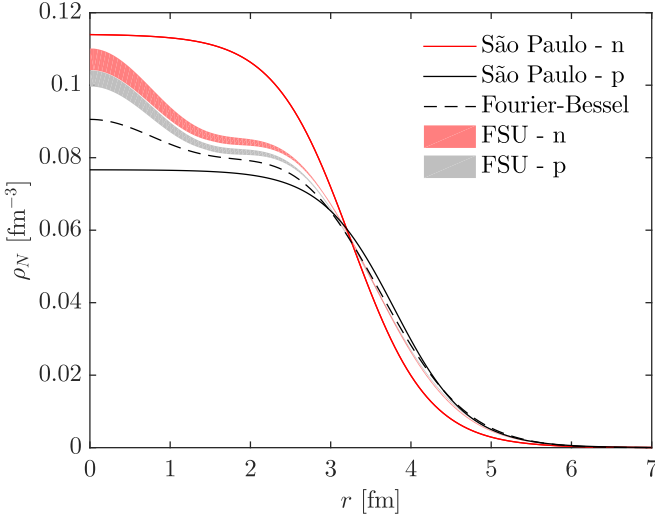


FIG. 3. Nucleonic densities of  $^{40}\text{Ca}$ : São Paulo parametrization (solid lines) [27], Fourier-Bessel expansion (dashed line) [29], and FSU relativistic mean-field calculations (bands) [30]. In the case of the Fourier-Bessel case, we assume  $\rho_n = \rho_p$ .

thickness. Given that the charge radius of  $^{40}\text{Ca}$  was incorporated into the calibration of the FSU model, its predictions at intermediate to large distances are close to those obtained from the Fourier-Bessel expansion [29]. With the exception of the Fourier-Bessel expansion, for which we again assume that  $\rho_n = \rho_p$ , all models predict negative neutron skin thicknesses. The first line of Table I lists these predictions. The negative value of the neutron skin thickness of  $^{40}\text{Ca}$  is not uncommon given that the Coulomb repulsion pushes protons out to the surface: this has also been found by Hagen *et al.* in their recent *ab initio* coupled cluster calculation [31,32]. However, the value obtained with the São Paulo parametrization is unrealistically large. Nevertheless, such a large spread in the model predictions will enable us to test the sensitivity of  $\pi^0$  photoproduction to the neutron density.

For the heavy  $^{208}\text{Pb}$  target, the sole charge density inferred from electron scattering is of little help in estimating the neutron density. Accordingly, only the São Paulo and FSU densities are considered; they are displayed in Fig. 4 as solid lines and bands, respectively. As for  $^{40}\text{Ca}$ , those bands correspond to the most extreme variation in the FSU model that still predicts the correct  $^{208}\text{Pb}$  binding energy—and in general all observables dominated by the isoscalar sector. In this case, the agreement between both models is better than for  $^{40}\text{Ca}$ , although the São Paulo neutron density continues to decay faster relative to the FSU predictions, leading to a

TABLE I. Neutron skin thicknesses for  $^{40}\text{Ca}$  and  $^{208}\text{Pb}$  predicted by the São Paulo parametrization [27] and the FSU relativistic mean-field calculations [30].

Model	São Paulo	FSU
$^{40}\text{Ca}$	-0.301 fm	[-0.051, -0.049] fm
$^{208}\text{Pb}$	0.101 fm	[0.176, 0.286] fm

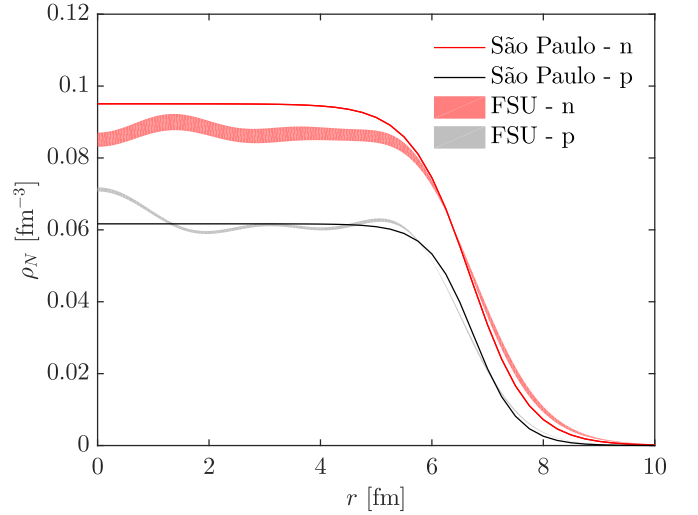


FIG. 4. Nuclear densities of  $^{208}\text{Pb}$ : São Paulo parametrization (solid lines) [27] and FSU relativistic mean-field calculations (bands) [30]. The neutron densities are shown in red and the proton ones in black or gray.

neutron skin thickness of about 0.1 fm, which is inconsistent with the extracted value from PREX-2. The significant spread of nearly 0.1 fm in the FSU predictions for  $^{208}\text{Pb}$  shown in Table I will be particularly valuable for our analysis of the  $\pi^0$ -photoproduction reaction—and the unrealistically small neutron skin thickness predicted by the São Paulo parametrization will enable us to extend our tests to even more extreme nucleonic densities.

### B. Plane- and distorted-wave impulse approximation calculations of $\pi^0$ photoproduction

The  $\pi^0$ -photoproduction cross section for a 200 MeV photon impinging on a  $^{12}\text{C}$  target is displayed in Fig. 5 as a function of the scattering angle  $\theta$  in the  $\pi$ - $A$  center-of-momentum frame. The PWIA [Fig. 5(a)] and DWIA [Fig. 5(b)] results presented in Sec. II are compared with the experimental data of Ref. [18].<sup>1</sup> We consider the three sets of model densities shown in Fig. 2 following the same line-type convention.

As is visible in Fig. 5(a), the PWIA cross sections are in a good agreement with the data without any adjustment of parameters. Not only is the predicted shape similar to the experimental one, with a maximum around  $50^\circ$ , but its magnitude is also in agreement with experiment. Our calculations exhibit a rather small sensitivity to the choice of density: despite the clear differences noted in Fig. 2, the corresponding  $\pi^0$ -photoproduction cross sections are very close to one another with the theoretical spread considerably

<sup>1</sup>Note that these data are extracted directly from Fig. 4 of Ref. [18]. For some of these data points, the error bars are not visible in the figure because they are occulted by the dots representing the data. For these points, we have made the conservative hypothesis that the data uncertainty is as large as the size of the dots.

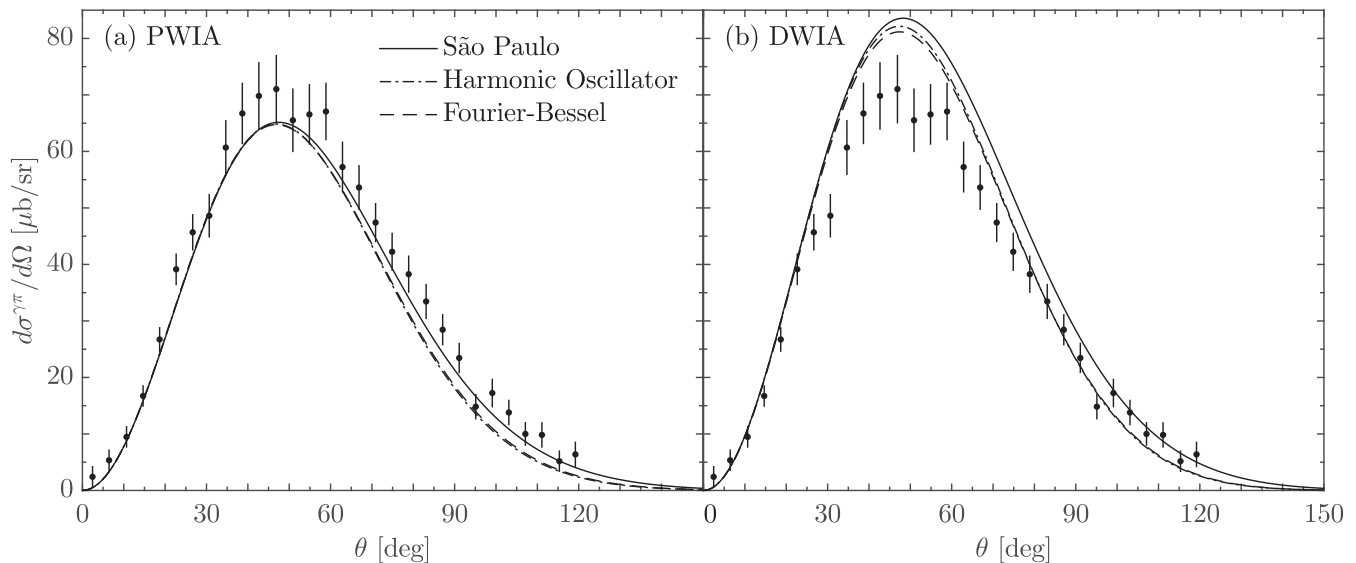


FIG. 5. Coherent  $\pi^0$  photoproduction cross section on a  $^{12}\text{C}$  target for a 200 MeV incident photon. The calculations are shown within the (a) PWIA and (b) DWIA versions of the model presented in Sec. II using the densities displayed in Fig. 2: the São Paulo (solid line), HO (dash-dotted line), and FB (dashed line) densities. Experimental data are from Ref. [18].<sup>1</sup>

smaller than the experimental error [18]. We note that the most compact spatial distribution, namely, the one obtained with the São Paulo parametrization, leads to the cross section that extends to the largest angles. This is to be expected since the  $\pi^0$ -photoproduction amplitude listed in Eq. (3) varies linearly with the Fourier transform of the nucleonic densities. The very similar HO and FB densities lead to nearly indistinguishable  $\pi^0$ -photoproduction cross sections.

When the reaction is calculated including final-state interactions [Fig. 5(b)], the photoproduction cross section increases by about 25%. Although the agreement is not as good as with the PWIA, such a significant enhancement confirms that pionic distortions cannot be neglected [16,21]. The energy dependence of the  $\pi$ - $A$  optical potential might be the cause for the observed disagreement. Another possibility is the role played by higher-order effects, as emphasized in Ref. [20]. Notably, pionic distortions seem to influence only the magnitude of the cross section; there is no significant change in the shape of the theoretical cross sections. That the DWIA cross section is proportional to the PWIA one is reminiscent of what has been observed in Ref. [33], where the effect of distortion on coherent  $\pi^0$  photoproduction has been analyzed for light targets and at energies near threshold, i.e., below 200 MeV. At the peak of the cross section, we can note some minor changes in the spreading of the theoretical predictions, suggesting that the choice of nuclear density is fairly insensitive to final-state interactions.

Figures 6(a) and 6(b) display the  $\pi^0$ -photoproduction cross section for a 200 MeV photon impinging on a  $^{40}\text{Ca}$  nucleus, without and with the inclusion of pionic distortions, respectively. The theoretical predictions are compared with the experimental data of Ref. [18]. On this heavier target, the nuclear form factor falls faster, resulting in a cross section that is more forward focused than in  $^{12}\text{C}$ , with the maximum located at  $\theta \approx 30^\circ$ . As in the case of  $^{12}\text{C}$ , the shape and absolute magnitude are better reproduced by the PWIA calculations.

We also note the appearance of a minimum in the data at about  $70^\circ$  followed by a second broad maximum. Such behavior is only qualitatively reproduced by our calculations: without distortions, all three choices of density predict a node between  $80^\circ$  and  $90^\circ$  followed by a tiny bump. In turn, pionic distortions fill the node, resulting in a slight increase of the height of the second maximum.

These features—viz. more forward-focussed cross section and the emergence of a minimum—can be easily interpreted in the PWIA remembering that the  $T$  matrix in Eq. (3) is proportional to the Fourier transform of the nuclear densities defined in Eq. (4). When the target mass increases, so does the radial extension of the nuclear density, whose Fourier transform accordingly peaks at smaller momentum  $q$ . The zero observed in the PWIA calculations corresponds to the first zero of  $\mathcal{F}[\rho]$ .

The differences observed in the cross sections computed with the three densities can also be easily interpreted following this line of thought. The spatial density that extends the farthest, i.e., the charge density described by a Fourier-Bessel expansion (see Fig. 3), produces the cross section that peaks at the most forward angle. It is then followed by the FSU band, whose densities are slightly less extended. The São Paulo parametrization, which predicts a very narrow neutron density, in turn leads to the cross section that extends to the largest angles. Note, however, that these differences in the cross section remain small despite the large discrepancy observed between the nucleonic densities in Fig. 3. The differences in the model are of the order of the experimental uncertainty, so it would be difficult to identify an optimal density choice solely based on these data.

As mentioned before, the distortion induced by the  $\pi^0$ - $A$  interaction significantly increases the theoretical predictions in the first peak in a way that seems independent of the nuclear density. Around the first maximum, we observe a uniform enhancement of the DWIA cross section by about 35% relative

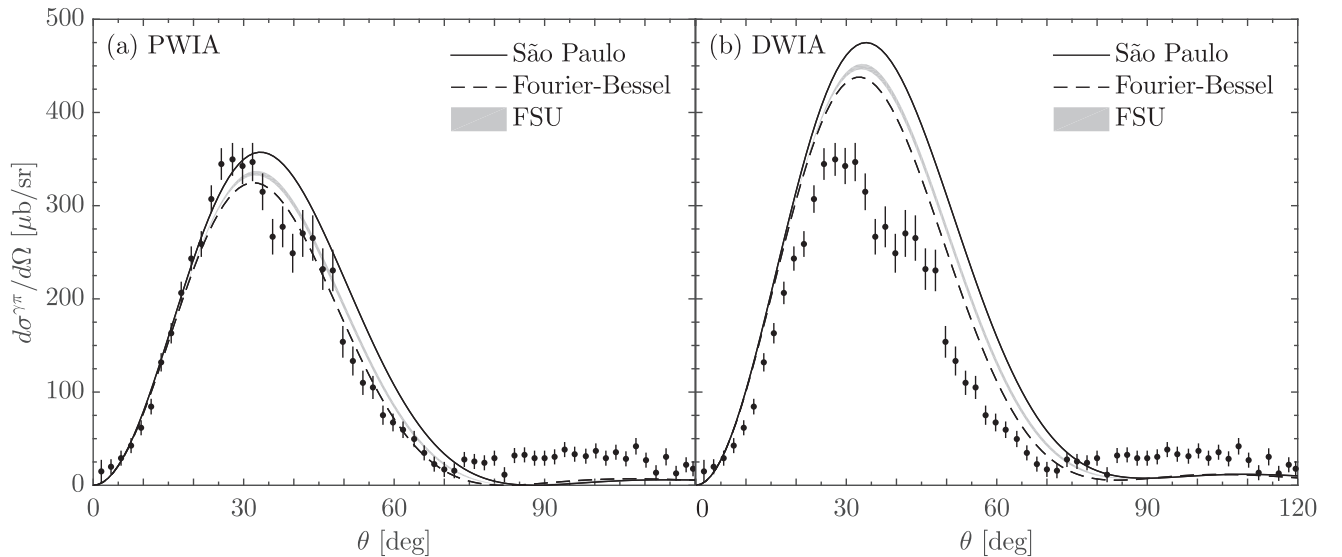


FIG. 6. Cross section for the  $\pi^0$  photoproduction of a 200 MeV photon impinging on  $^{40}\text{Ca}$  computed at (a) the PWIA and (b) the DWIA. The calculations use the three densities presented in Fig. 3: the São Paulo Fermi-Dirac density (solid line), Fourier-Bessel expansion of the charge density (dashed line), and the relativistic mean-field FSU calculation (gray band). Experimental data are from Ref. [18].

to the PWIA prediction. At larger angles, the effect of the distortion effects is no longer linear. Distortions smear the PWIA curves in the region of their node and enhances the second maximum, however, not enough to reach the experimental data. The disagreement with the data on  $^{40}\text{Ca}$  is stronger than for  $^{12}\text{C}$ . Part of the problem may again be due to the parameters of the MSU potential or to higher-order effects neglected in this IA approach [20]. Another major source of uncertainty is of experimental nature: in the case of  $^{40}\text{Ca}$ , it was difficult to isolate the purely coherent events from the incoherent ones [34]. Nevertheless, this test enables us to confirm that our model provides sensible results, that distortions play a non-negligible role, and, most importantly, that this observable depends little on the choice of the nuclear density.

The  $\pi^0$ -photoproduction cross section on  $^{208}\text{Pb}$  induced by a 200 MeV photon is presented in Fig. 7. Both PWIA and DWIA calculations are compared against the experimental data of Ref. [18].<sup>2</sup> We consider the two density choices presented in Fig. 4.

The changes observed for the lead target follow closely the insights developed earlier. The cross section on such a heavy nucleus peaks at even more forward angles, with the first maximum at  $\theta \approx 18^\circ$  and a first minimum at about  $40^\circ$ ; a second maximum is now clearly visible at  $55^\circ$  followed by a second minimum and the shadow of a subsequent third maximum beyond  $80^\circ$ . Given that these features are encoded

in the nucleonic form factors, they are already evident at the PWIA level. Indeed, the first and second experimental peaks [18] are well reproduced both in location and magnitude. The first minimum is also well reproduced, although the theoretical cross section reaches zero where the Fourier transform of the nucleonic density vanishes. Once again, we observe a rather small difference between the model densities that is easy to understand: given that the São Paulo densities decay faster than the FSU ones, the associated cross section is shifted to slightly larger angles (see Fig. 4).

As was the case for  $^{12}\text{C}$  and  $^{40}\text{Ca}$ , introducing pionic final-state interactions leads to an increase in the cross section in the first peak. However, in this case, accounting for distortion effects *improves* the description of the experimental data. The magnitude of the first peak predicted by the DWIA calculations is in excellent agreement with the experiment. Moreover, the smearing of the first node is such that our theoretical cross sections now fall directly on the data. It is interesting to note that the differences observed at the PWIA between the two sets of nucleonic densities is reduced when distortions are included, so that both calculations agree nearly perfectly with the data. Given that these calculations have been performed without any adjustment of parameters, it is gratifying to see such an excellent description of the experimental data [18]. Relative to the lighter targets, the excellent agreement observed here may be due to the fact that the IA may be better suited for heavy targets.

Since both sets of nuclear densities provide a nearly perfect description of the experimental data, it is clear that no reliable nuclear structure information can be obtained solely from this experiment. This result has a profound implication on the use of coherent  $\pi^0$  photoproduction to infer the neutron skin thickness of heavy nuclei. As shown in Fig. 7(b), using very different nucleonic densities—from the purely phenomenological São Paulo parametrization to a range of relativistic mean-field models—we observe no significant differences in

<sup>2</sup>Unfortunately, we are unable to directly compare our results to the data of Tarbert *et al.* [19] because of an inconsistency in the presentation of this more recent measurement on  $^{208}\text{Pb}$ , see Ref. [20]. However, we were told [34] that, with a proper scaling, they are in excellent agreement with the previous data of Krusche *et al.* [18]. Accordingly, we infer that this new set of data does not change the conclusion of our study.

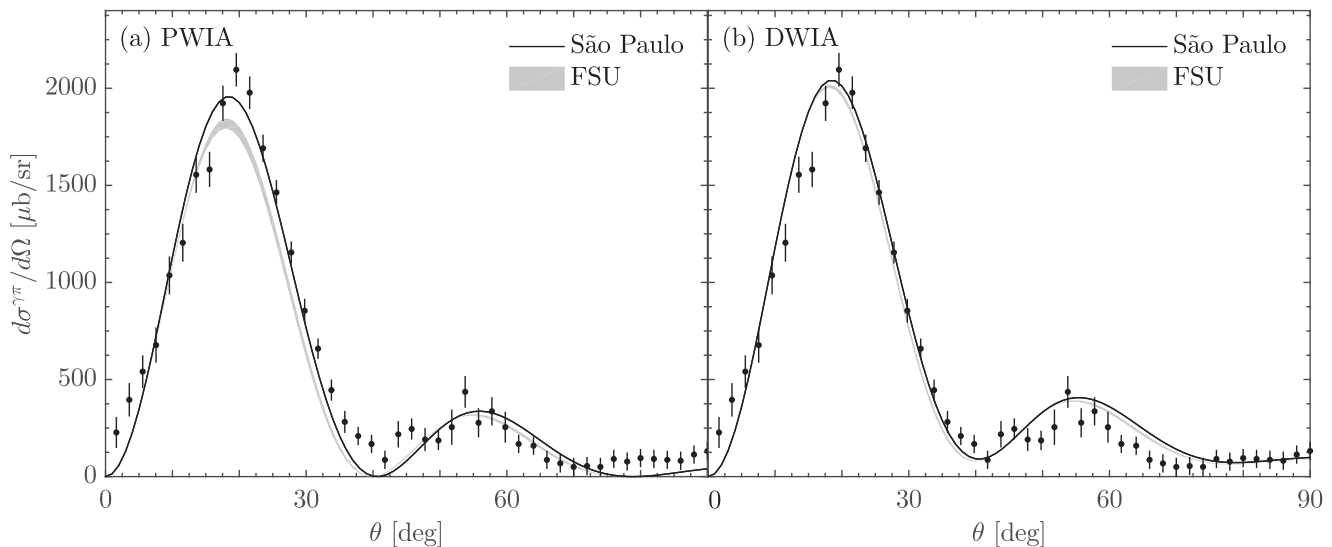


FIG. 7. Cross section for the  $\pi^0$  photoproduction cross section on  $^{208}\text{Pb}$  by a 200 MeV photon. The calculations performed at (a) the PWIA and (b) the DWIA are presented for the São Paulo density (solid line) and using the results of the FSU relativistic mean-field calculations (gray band). Experimental data are from Ref. [18].

our predictions for  $^{208}\text{Pb}$ . This finding is in stark disagreement with the result reported in Ref. [19] that suggests that the neutron skin thickness of  $^{208}\text{Pb}$  can be extracted with an astounding precision of  $R_{\text{skin}}^{208} = 0.15 \pm 0.03(\text{stat.})_{-0.03}^{+0.01}(\text{syst.})$  fm. In contrast, our analysis indicates that this photoproduction reaction cannot distinguish between theoretical models for which the neutron skin thickness in  $^{208}\text{Pb}$  differs by at least 0.2 fm. We note that this interval is likely a lower bound since calculations performed with values outside the adopted range may still provide an equally good description of the experimental data. Beyond this systematic uncertainty, one should also take into account various higher-order effects that are not included within the framework of the impulse approximation. For example, Miller shows that although small, these effects can result in an additional theoretical uncertainty of up to 6%, which can falsify the inferred neutron skin thickness by up to 50% [20].

Our analysis indicates that the coherent photoproduction amplitude is largely isoscalar. That is, the cross section is sensitive to the whole (neutron + proton) density and bears little dependence on the differences in densities. Accordingly, this reaction is not suitable to constrain any isovector observable, such as the neutron skin thickness. Perhaps comparing  $\pi^0$ -photoproduction cross sections along a long chain of stable isotopes may provide a better constraint on  $R_{\text{skin}}$ . We explore this possibility in the following section.

#### IV. PREDICTIONS FOR $\pi^0$ PHOTOPRODUCTION ON $^{116,124}\text{Sn}$

Tin exhibits the longest chain of stable isotopes in the nuclear chart, so it would be interesting to examine how the neutron skin thickness evolves with increasing neutron number. Inspired by the precision claimed in Ref. [19], an experimental campaign has been started at MAMI, the Mainz

Microtron of the Johannes Gutenberg University Mainz [35], to measure the coherent  $\pi^0$  photoproduction on three stable isotopes  $^{116}\text{Sn}$ ,  $^{120}\text{Sn}$ , and  $^{124}\text{Sn}$ . In this section we apply our theoretical framework to the lightest and heaviest of these isotopes to (a) assess how changes in the nuclear density, especially in the neutron skin thickness, affect the  $\pi^0$  photoproduction cross sections for each of these two nuclei and (b) to estimate the experimental precision required to resolve the expected differences in the neutron skin thickness of these two nuclei. The measurements have been carried out in a range of incoming photon energies between 140 and 300 MeV. Since the extraction of coherent events is optimized within the 180–190 MeV energy bin, we focus on this particular energy range, which is compatible with the MSU potential used to describe the final  $\pi^0$ -nucleus interaction [25].

As in the case of  $^{208}\text{Pb}$ , we consider nucleonic densities obtained from both the phenomenological São Paulo [27] and FSU [30] parametrizations. As done earlier, we consider the same set of relativistic mean-field models to produce a set of physically meaningful densities that will generate a broad range of neutron skin thickness. These density profiles are displayed in Figs. 8(a) and 8(b) for  $^{116}\text{Sn}$  and  $^{124}\text{Sn}$ , respectively. The São Paulo parametrization is shown with solid lines and the range of FSU predictions is shown as bands; the black or gray lines correspond to proton densities and the red ones to neutron densities. The São Paulo potential predicts a profile that decays faster with  $r$  than the mean-field calculations, especially in the case of the neutron densities. We note that the interior depression in  $^{116}\text{Sn}$ , the so-called “nuclear bubble” [36,37], is due to an empty  $3s^{1/2}$  neutron orbital that is only 0.4 MeV below the fully occupied  $2d^{3/2}$  orbital. We expect that the bubble will be partially filled by the inclusion of pairing correlations which are absent from our model. In the case of  $^{124}\text{Sn}$ , both of these neutron orbitals are filled so the bubble disappears. The neutron skin thickness deduced from these densities can be found in Table II. Based on the São



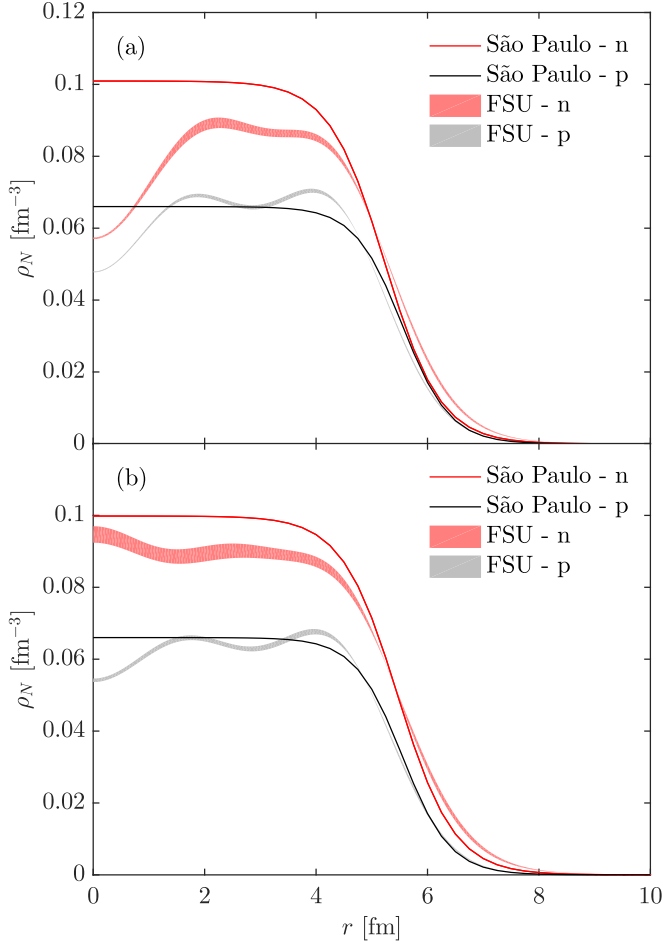


FIG. 8. Neutron (red) and proton (black or gray) densities for (a)  $^{116}\text{Sn}$  and (b)  $^{124}\text{Sn}$ . São Paulo (solid lines) [27] and FSU (bands) [30] densities are displayed.

Paulo density profiles shown in Fig. 8, the São Paulo potential predicts a negative neutron skin thickness for  $^{116}\text{Sn}$  and a very thin one for  $^{124}\text{Sn}$ . In contrast, the FSU parametrization predicts significantly thicker neutron skins and illustrates the clear impact of adding eight more neutrons in going from  $^{116}\text{Sn}$  to  $^{124}\text{Sn}$ .

Our calculated cross sections are presented in Fig. 9. The top panels correspond to the  $^{116}\text{Sn}$  target with calculations performed in the plane-wave impulse approximation [Fig. 9(a)] and distorted-wave impulse approximation [Fig. 9(b)]; the bottom panels show the corresponding results for  $^{124}\text{Sn}$ . As expected, the main features of these results can be readily understood from the analysis presented in the previous section. First, with a first maximum between  $22^\circ$  and  $23^\circ$  and a first minimum at about  $50^\circ$ , the angular distributions

on the tin isotopes, while more forward focused than on  $^{40}\text{Ca}$ , spread to larger angles than on  $^{208}\text{Pb}$ . We note that if the nuclear density could be faithfully approximated by a *symmetrized* Fermi-Dirac shape—which is practically identical to the conventional Fermi-Dirac shape—the associated form factor is known analytically [38]. Such an analytic approach encapsulates the main features displayed by the cross section, namely, diffractive oscillations controlled by the half-density radius modulated by an exponential falloff controlled by the surface thickness. Second, whereas Fig. 8 suggests significant differences in the predictions of the nuclear-structure models for the proton and neutron densities, the sensitivity of the cross section to the choice of density profile is rather small. The minor changes observed between the cross sections computed with the São Paulo and FSU densities can once more be traced back to their Fourier transform: the São Paulo parametrization, predicting a more compact density profile, leads to a slightly more extended  $\pi^0$ -photoproduction cross section than the FSU calculations. That is, despite the significant differences in the predictions for the neutron skin thickness (see Table II) the minimum in the cross section suggested by the São Paulo parametrization is shifted to a slightly larger angle relative to the FSU predictions. Third, the inclusion of final-state interactions [Figs. 9(b) and 9(d)] has a significant effect: it increases the cross section at all angles although not uniformly; for example, the first and second minima are filled whereas the increase in the first peak is about 10%. Moreover, as for  $^{208}\text{Pb}$ , we observe a clear reduction of the relative difference between the calculations performed with the São Paulo and the FSU densities. This is especially noticeable in Fig. 9(b) for the case of  $^{116}\text{Sn}$ , for which the pionic distortions wash away most of the differences. The third point confirms that, once the  $\pi^0$ -nucleus interaction is accounted for in the outgoing channel, all densities—despite their significant differences—provide very similar cross sections. In the particular case of the more realistic FSU densities, which cover a range of neutron skin thicknesses of about 0.07 fm for  $^{116}\text{Sn}$  and 0.1 fm for  $^{124}\text{Sn}$ , the differences in our DWIA cross sections do not even reach 1.5% at the first maximum for either isotope. These results suggest that, even if the experiments could reach a 1.5% precision, the neutron skin thickness could not be determined to better than 0.07 fm for  $^{116}\text{Sn}$  and 0.1 fm for  $^{124}\text{Sn}$ .

Because of the small overall difference in size between both isotopes, we observe a slight shift towards forward angles of the  $\pi^0$ -photoproduction cross section from  $^{116}\text{Sn}$  to  $^{120}\text{Sn}$ . This isotopic shift varies slightly with the choice of the density. However, as for the aforementioned difference in magnitude, the model dependence is reduced at the DWIA level. To resolve such a minor shift in order to get some information on the difference in neutron skin thickness between both targets, an experimental precision of at least  $1.5^\circ$  is required. Perhaps a combination of these cross sections, such as a relative difference, might enable us to infer a more reliable estimate of the change in neutron skin thickness between the tin isotopes. However, as already seen in Sec. III, under the present experimental conditions, it is unrealistic to use this sole reaction observable to infer the absolute neutron skin thickness of these nuclei. Ultimately, it is the fact that the

TABLE II. Neutron skin thicknesses for  $^{116}\text{Sn}$  and  $^{124}\text{Sn}$ .

Model	São Paulo	FSU range
$^{116}\text{Sn}$	-0.035 fm	[0.104, 0.170] fm
$^{124}\text{Sn}$	0.013 fm	[0.188, 0.284] fm

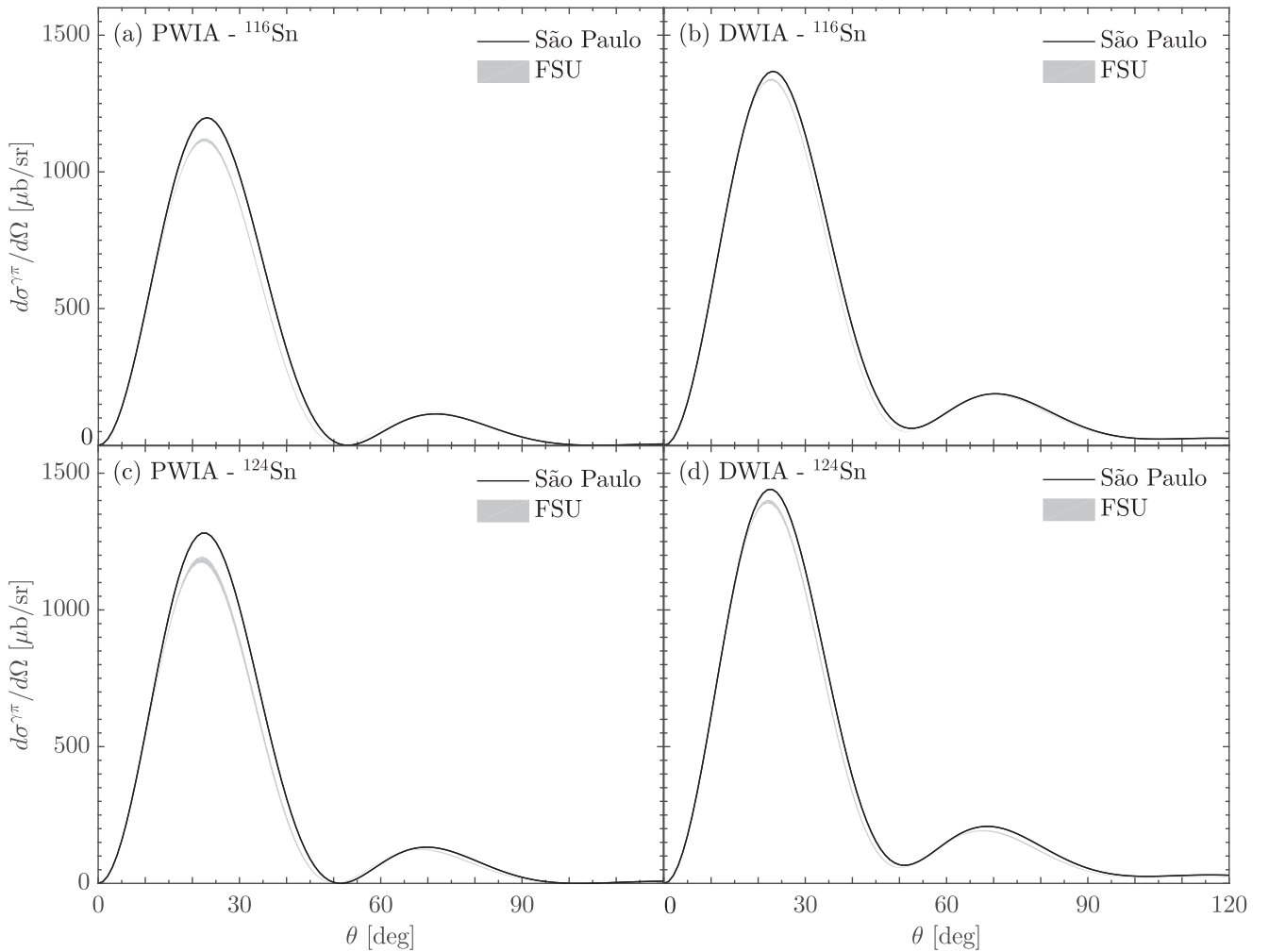


FIG. 9. Coherent  $\pi^0$  photoproduction cross section for a 200 MeV photon impinging on  $^{116}\text{Sn}$  (top panels) and  $^{124}\text{Sn}$  (bottom panels). The calculations are performed at the (a), (c) PWIA and at the (b), (d) DWIA by using the density profiles shown in Fig. 8: the São Paulo parametrization (solid line) and the prediction of the FSU relativistic mean-field model (gray band).

$\pi^0$ -photoproduction reaction is mostly sensitive to the *isoscalar* density that makes the extraction of the isovector neutron skin thickness so challenging.

## V. CONCLUSION

Coherent  $\pi^0$  photoproduction has been suggested as an accurate probe of the nuclear shape with sufficient sensitivity to determine the thickness of the neutron skin [19]. In this work, we test this assertion by performing calculations of the  $\pi^0$ -photoproduction cross section using a distorted-wave impulse approximation framework to compare against existing and future experimental data. We consider  $^{12}\text{C}$ ,  $^{40}\text{Ca}$ ,  $^{116,124}\text{Sn}$ , and  $^{208}\text{Pb}$  as targets and use a variety of nucleonic densities to test the sensitivity of the cross section to the neutron skin thickness.

We observe a general good agreement with the data of Ref. [18]. For the light targets  $^{12}\text{C}$  and  $^{40}\text{Ca}$  we reproduce the shape and order of magnitude of the experimental cross section. In the case of  $^{208}\text{Pb}$ , the agreement is nearly perfect without resorting to any parameter fitting, probably because

the impulse approximation and a mean-field description of nuclear densities are better suited for heavier targets. As observed in Refs. [16,18], the effect of final-state interactions is significant so it cannot be ignored. Pionic distortions lead to an increase of the cross section, which is largest on the light targets. Moreover, final-state interactions are largely insensitive to the choice of nuclear density. In general—and particularly for the heavier targets—such an effect tends to *reduce* the sensitivity of the  $\pi^0$ -photoproduction cross section to the nuclear density.

The major result of this work is that the photoproduction of a neutral pion on a nucleus is largely insensitive to the nuclear density. In the case of  $^{208}\text{Pb}$ , using densities generated from a relativistic mean-field model [30] produces a cross section that is practically indistinguishable from the one obtained using a simple Fermi-Dirac parametrization that predicts a very small neutron skin [27]; such a small neutron skin has now been ruled out by experiment [8]. In essence, given that the photoproduction cross section is dominated by the isoscalar ( $\rho_n + \rho_p$ ) density, it is difficult to extract an isovector observable—such as the neutron skin thickness—

with enough precision to provide meaningful constraints on the density dependence of the symmetry energy. Indeed, our analysis shows that, for the fairly wide range of neutron skin thickness adopted in this work, i.e.,  $R_{\text{skin}}^{208} \approx (0.1\text{--}0.3)$  fm, all models reproduce the experimental data of Ref. [18] equally well, without any adjustment of model parameters.

Our results challenge the main conclusion derived from a similar experiment that suggests that the neutron skin thickness of  $^{208}\text{Pb}$  can be determined with a total (statistical + systematic) uncertainty of only  $\approx 0.04$  fm [19]. Given that the  $\pi^0$ -photoproduction reaction is unable to provide a reliable estimate of the neutron skin thickness, the method cannot shed any light on the discrepancy observed by the various estimates of  $R_{\text{skin}}^{208}$  reported in the literature [1,3].

The extension of this study to  $^{116}\text{Sn}$  and  $^{124}\text{Sn}$ —for which the  $\pi^0$  photoproduction has already been measured at Mainz—leads to similar conclusions, confirming that this reaction is largely insensitive to the thickness of the neutron

skin. Hence, these measurements alone are not sufficient to estimate accurately the evolution of the neutron skin thickness along that isotopic chain as initially hoped. A combination of different measurements, like a relative difference of cross sections measured on two extreme isotopes may help validate the idea behind the method.

## ACKNOWLEDGMENTS

We are grateful to the late B. Krusche for discussions about the analysis of pertinent experimental data. This work was supported by the PRISMA+ (Precision Physics, Fundamental Interactions and Structure of Matter) Cluster of Excellence and the Deutsche Forschungsgemeinschaft (DFG, German Research Foundation) under the Project-ID 204404729 (SFB 1044). J.P. acknowledges support by the U.S. Department of Energy Office of Science, Office of Nuclear Physics under Award No. DE-FG02-92ER40750.

- 
- [1] M. B. Tsang, J. R. Stone, F. Camera, P. Danielewicz, S. Gandolfi, K. Hebeler, C. J. Horowitz, J. Lee, W. G. Lynch, Z. Kohley, R. Lemmon, P. Möller, T. Murakami, S. Riordan, X. Roca-Maza, F. Sammarruca, A. W. Steiner, I. Vidaña, and S. J. Yennello, *Phys. Rev. C* **86**, 015803 (2012).
- [2] C. J. Horowitz, E. F. Brown, Y. Kim, W. G. Lynch, R. Michaels, A. Ono, J. Piekarewicz, M. B. Tsang, and H. H. Wolter, *J. Phys. G* **41**, 093001 (2014).
- [3] M. Thiel, C. Sfienti, J. Piekarewicz, C. J. Horowitz, and M. Vanderhaeghen, *J. Phys. G* **46**, 093003 (2019).
- [4] J. M. Lattimer and M. Prakash, *Phys. Rep.* **442**, 109 (2007).
- [5] C. J. Horowitz and J. Piekarewicz, *Phys. Rev. Lett.* **86**, 5647 (2001).
- [6] C. J. Horowitz and J. Piekarewicz, *Phys. Rev. C* **64**, 062802(R) (2001).
- [7] S. Abrahamyan, Z. Ahmed, H. Albatineh, K. Aniol, D. S. Armstrong, W. Armstrong, T. Averett, B. Babineau, A. Barbieri, V. Bellini, R. Beminiwattha, J. Benesch, F. Benmokhtar, T. Bielarski, W. Boeglin, A. Camsonne, M. Canan, P. Carter, G. D. Cates, C. Chen, and P. Zhu (PREX Collaboration), *Phys. Rev. Lett.* **108**, 112502 (2012).
- [8] D. Adhikari, H. Albatineh, D. Androic, K. Aniol, D. S. Armstrong, T. Averett, C. Ayerbe Gayoso, S. Barcus, V. Bellini, R. S. Beminiwattha, J. F. Benesch, H. Bhatt, D. Bhatta Pathak, D. Bhetuwal, B. Blaikie, Q. Campagna, A. Camsonne, G. D. Cates, Y. Chen, C. Clarke, and X. Zheng (PREX Collaboration), *Phys. Rev. Lett.* **126**, 172502 (2021).
- [9] J. Zenihiro, H. Sakaguchi, T. Murakami, M. Yosoi, Y. Yasuda, S. Terashima, Y. Iwao, H. Takeda, M. Itoh, H. P. Yoshida, and M. Uchida, *Phys. Rev. C* **82**, 044611 (2010).
- [10] A. Trzcíńska, J. Jastrzębski, P. Lubiński, F. J. Hartmann, R. Schmidt, T. von Egidy, and B. Kłos, *Phys. Rev. Lett.* **87**, 082501 (2001).
- [11] B. Kłos, A. Trzcíńska, J. Jastrzębski, T. Czosnyka, M. Kisieliński, P. Lubiński, P. Napiorkowski, L. Pieńkowski, F. J. Hartmann, B. Ketzer, P. Ring, R. Schmidt, T. von Egidy, R. Smolańczuk, S. Wycech, K. Gulda, W. Kurcewicz, E. Widmann, and B. A. Brown, *Phys. Rev. C* **76**, 014311 (2007).
- [12] A. Tamii, I. Poltoratska, P. von Neumann-Cosel, Y. Fujita, T. Adachi, C. A. Bertulani, J. Carter, M. Dozono, H. Fujita, K. Fujita, K. Hatanaka, D. Ishikawa, M. Itoh, T. Kawabata, Y. Kalmykov, A. M. Krumbholz, E. Litvinova, H. Matsubara, K. Nakanishi, R. Neveling *et al.*, *Phys. Rev. Lett.* **107**, 062502 (2011).
- [13] P.-G. Reinhard and W. Nazarewicz, *Phys. Rev. C* **81**, 051303(R) (2010).
- [14] R. A. Schrack, J. E. Leiss, and S. Penner, *Phys. Rev.* **127**, 1772 (1962).
- [15] J. E. Leiss and R. A. Schrack, *Rev. Mod. Phys.* **30**, 456 (1958).
- [16] D. Drechsel, L. Tiator, S. Kamalov, and S. N. Yang, *Nucl. Phys. A* **660**, 423 (1999).
- [17] G. Fricke, C. Bernhardt, K. Heilig, L. Schaller, L. Schellenberg, E. Spera, and C. Dejager, *At. Data Nucl. Data Tables* **60**, 177 (1995).
- [18] B. Krusche, J. Ahrens, R. Beck, S. Kamalov, V. Metag, R. Owens, and H. Ströher, *Phys. Lett. B* **526**, 287 (2002).
- [19] C. M. Tarbert, D. P. Watts, D. I. Glazier, P. Aguar, J. Ahrens, J. R. M. Annand, H. J. Arends, R. Beck, V. Bekrenev, B. Boillat, A. Braghieri, D. Branford, W. J. Briscoe, J. Brudvik, S. Cherepnaya, R. Codling, E. J. Downie, K. Foehl, P. Grabmayr, R. Gregor, and F. Zehr (Crystal Ball at MAMI and A2 Collaborations), *Phys. Rev. Lett.* **112**, 242502 (2014).
- [20] G. A. Miller, *Phys. Rev. C* **100**, 044608 (2019).
- [21] W. Peters, H. Lenske, and U. Mosel, *Nucl. Phys. A* **640**, 89 (1998).
- [22] G. F. Chew, M. L. Goldberger, F. E. Low, and Y. Nambu, *Phys. Rev.* **106**, 1345 (1957).
- [23] D. Drechsel, S. S. Kamalov, and L. Tiator, *Eur. Phys. J. A* **34**, 69 (2007).
- [24] M. Gmitro, J. Kvasil, and R. Mach, *Phys. Rev. C* **31**, 1349 (1985).
- [25] J. A. Carr, H. McManus, and K. Stricker-Bauer, *Phys. Rev. C* **25**, 952 (1982).
- [26] M. Ericson and T. Ericson, *Ann. Phys. (NY)* **36**, 323 (1966).

- [27] L. C. Chamon, B. V. Carlson, L. R. Gasques, D. Pereira, C. De Conti, M. A. G. Alvarez, M. S. Hussein, M. A. Cândido Ribeiro, E. S. Rossi, and C. P. Silva, *Phys. Rev. C* **66**, 014610 (2002).
- [28] C. De Jager, H. De Vries, and C. De Vries, *At. Data Nucl. Data Tables* **14**, 479 (1974).
- [29] B. Dreher, J. Friedrich, K. Merle, H. Rothhaas, and G. Lührs, *Nucl. Phys. A* **235**, 219 (1974).
- [30] B. G. Todd-Rutel and J. Piekarewicz, *Phys. Rev. Lett.* **95**, 122501 (2005).
- [31] G. Hagen, A. Ekström, C. Forssén, G. R. Jansen, W. Nazarewicz, T. Papenbrock, K. A. Wendt, S. Bacca, N. Barnea, B. Carlsson, C. Drischler, K. Hebeler, M. Hjorth-Jensen, M. Miorelli, G. Orlandini, A. Schwenk, and J. Simonis, *Nat. Phys.* **12**, 186 (2016).
- [32] G. Hagen (private communication).
- [33] A. A. Chumbalov, R. A. Eramzhyan, and S. S. Kamalov, *Z. Phys. A* **328**, 195 (1987).
- [34] B. Krusche (private communication).
- [35] K.-H. Kaiser, K. Aulenbacher, O. Chubarov, M. Dehn, H. Euteneuer, F. Hagenbuck, R. Herr, A. Jankowiak, P. Jennewein, H.-J. Kreidel, U. Ludwig-Mertin, M. Negrazus, S. Ratschow, S. Schumann, M. Seidl, G. Stephan, and A. Thomas, *Nucl. Instrum. Methods Phys. Res. Sect. A* **593**, 159 (2008).
- [36] B. G. Todd-Rutel, J. Piekarewicz, and P. D. Cottle, *Phys. Rev. C* **69**, 021301(R) (2004).
- [37] M. Grasso, L. Gaudefroy, E. Khan, T. Nikšić, J. Piekarewicz, O. Sorlin, N. Van Giai, and D. Vretenar, *Phys. Rev. C* **79**, 034318 (2009).
- [38] J. Piekarewicz, A. R. Linero, P. Giuliani, and E. Chicken, *Phys. Rev. C* **94**, 034316 (2016).